




## Article

# Proton-Ion Conductivity in Hexagonal Wurtzite-Nanostructured ZnO Particles When Exposed to a Reducing Atmosphere

Jinpeng Li <sup>1</sup>, Naveed Mushtaq <sup>2</sup>, Naila Arshad <sup>3</sup> , M. A. K. Yousaf Shah <sup>2</sup> , Muhammad Sultan Irshad <sup>3</sup> , Rong Yan <sup>4</sup>, Senlin Yan <sup>5</sup> and Yuzheng Lu <sup>5,\*</sup>

<sup>1</sup> Department of Electronic Engineering, Huainan Union University, Huainan 232000, China

<sup>2</sup> Jiangsu Provincial Key Laboratory of Solar Energy Science and Technology/Energy Storage Joint Research Center, School of Energy and Environment, Southeast University, No. 2 Si Pai Lou, Nanjing 210096, China

<sup>3</sup> Guangdong Provincial Key Laboratory of Micro/Nano Optomechatronics Engineering, College of Mechatronics and Control Engineering, Shenzhen University, Shenzhen 518060, China

<sup>4</sup> Department of Electronic Engineering, Nanjing Vocational Institute of Mechatronic Technology, Nanjing 211135, China

<sup>5</sup> School of Electronic Engineering, Nanjing Xiaozhuang University, Nanjing 211171, China

\* Correspondence: luyuzheng@njztc.edu.cn

**Abstract:** Zinc oxide (ZnO), a direct wide band gap semiconductor ( $\geq 3.30$  eV), has widespread potential for applications in energy devices and related industries. The initial physical demonstration of ZnO in ceramic fuel cells (CFCs) gave a new view of developing high ionic conductivity for multifunctional semiconductor technology. However, in the present work, we successfully synthesized highly textured nanoparticles of ZnO using a hydrothermal method followed by sintering in a reducing atmosphere. The resultant ZnO materials as electrolytes showed efficient ionic conductivity ( $5.28 \times 10^{-2} \text{ S cm}^{-1}$ ) and an excellent power density of  $520 \text{ mW cm}^{-2} \pm 5\%$  at  $550^\circ\text{C}$  for low-temperature ceramic fuel cells (LT-CFCs). The achievement of enhanced ionic conductivity without any external ions or cation doping in the CFC was anticipated, since there was a rare possibility of vacancies in the bulk ZnO structure to conduct oxygen ions or protons. Therefore, we found that laterally the surfaces of the ZnO nanoparticles could be textured to become oxygen-deficient when sintered in an  $\text{H}_2$  atmosphere, which suggests a special mechanism for effective ionic transport. Furthermore, experimental analyses such as SEM, XPS, UV-visible, and EIS methods were performed to analyze the changes in the structural properties and mechanism of ionic transport in ZnO nanoparticles. The presented work provides insights into a novel approach for developing high ionic conductivity in electrolytes in low-cost semiconductor oxides such as ZnO for energy storage and conversion devices.



**Citation:** Li, J.; Mushtaq, N.; Arshad, N.; Shah, M.A.K.Y.; Irshad, M.S.; Yan, R.; Yan, S.; Lu, Y. Proton-Ion Conductivity in Hexagonal Wurtzite-Nanostructured ZnO Particles When Exposed to a Reducing Atmosphere. *Crystals* **2022**, *12*, 1519. <https://doi.org/10.3390/cryst12111519>

Academic Editor: Andreas Thissen

Received: 20 September 2022

Accepted: 19 October 2022

Published: 26 October 2022

**Publisher's Note:** MDPI stays neutral with regard to jurisdictional claims in published maps and institutional affiliations.



**Copyright:** © 2022 by the authors. Licensee MDPI, Basel, Switzerland. This article is an open access article distributed under the terms and conditions of the Creative Commons Attribution (CC BY) license (<https://creativecommons.org/licenses/by/4.0/>).

**Keywords:** hydrothermal method; ZnO nanoparticles; reducing atmosphere conditions; ionic transport; spectroscopic studies; LT-SOFCs

## 1. Introduction

The development of low-cost semiconductor oxides with optimized ionic conductivity (for oxides and protons) has attracted growing interest due to their widespread applications in solid oxide fuel cells (SOFCs) and proton ceramic fuel cells (PCFCs) [1]. Most often, yttria-stabilized zirconia (YSZ) is used as an electrolyte in state-of-the-art commercial SOFCs, which shows adequate ionic conductivity only at high temperatures ( $\geq 800^\circ\text{C}$ ), which creates many technical challenges in terms of material selection and long-term durability, restricting the widespread application of SOFC technology [2]. Developing an alternative electrolyte with good ionic conductivity at intermediate temperatures ( $400\text{--}700^\circ\text{C}$ ) is highly desirable [3]. Alternatively, doped barium cerates and zirconates-based perovskite oxides have attracted considerable attention for developing high proton conductivity at intermediate temperatures and have demonstrated high power outputs in PCFCs [4].

However, most proton-conducting electrolytes suffer from poor chemical stability, e.g., in CO<sub>2</sub>, H<sub>2</sub>, or H<sub>2</sub>O atmospheres. Recently, materials with dual-ion-conducting (O<sup>2-</sup>/H<sup>+</sup>) capabilities have been proposed as a new class of electrolytes for intermediate-temperature fuel cells, as they exhibit low ohmic resistance without external gas humidification [5–7].

The development of a new semiconductor oxide electrolyte for SOFCs has attracted much more interest. Compared to the traditional concept, semiconductor electrolytes have multiple functions and transport channels for protons, oxygen ions, and electrons or holes. The feasible application of semiconducting oxides as electrolytes has led to a new perspective and strategy for developing low-temperature SOFCs. Therefore, a series of semiconducting or semiconductor heterostructure electrolytes have been studied in the past several years [8–12]. ZnO has gained a great deal of attention for its use in wide direct energy band gap semiconductors with smaller dispersive energy bands. Following this, Xia et al. reported a p-n heterostructure of BaCo<sub>0.4</sub>Fe<sub>0.4</sub>Zr<sub>0.1</sub>Y<sub>0.1</sub>O<sub>3-δ</sub>-ZnO, which exhibited remarkable ionic conductivity performance in fuel cells operating at 450–500 °C [13]. In our latest study, we introduced a semiconductor heterostructure consisting of p-type SrFe<sub>0.2</sub>Ti<sub>0.8</sub>O<sub>3</sub> and n-type ZnO. It was evaluated as an electrolyte in LT-SOFCs by achieving a good peak power density of 650 mW cm<sup>-2</sup> at 520 °C [14]. In another work, Xia et al. reported high ionic conductivity and power outputs in Li-doped ZnO and La/Pr-doped CeO<sub>2</sub>-ZnO heterostructures [15,16]. These results mentioned above indicate the potential application of Zn electrolytes in a fuel cell that can achieve encouraging power densities at low operating temperatures of 450–550 °C, which are comparable to those used for thin-film SOFCs using pure ion-conducting electrolytes, e.g., YSZ.

However, the further control of the morphology and sintering conditions to achieve nanocrystalline semiconductor oxides has recently gained considerable attention. Therefore, in this study, we have synthesized ZnO nanoparticles with a potentially desirable morphology to regulate their electrical properties. The synthesis of ZnO was achieved by following the three preparation processes: (i) co-precipitation; (ii) hydrothermal techniques; (iii) dry freezing techniques. The as-prepared ZnO powder was studied via morphological, chemical, and structural analyses. The “surface locking” effect for the ion transport was introduced to explain the possible in situ defects in the ZnO surface layer upon exposure to H<sub>2</sub> in fuel cell conditions, which facilitates the ions’ migration, followed by internal cavity development (the accumulation and depletion region of charges). Spontaneous ionic transportation was recorded in the developed ZnO, revealing the optimum ionic conductivity rate (up to 5.28 × 10<sup>-2</sup> S cm<sup>-1</sup>) along with a power density of 520 mW cm<sup>-2</sup> when operating at 550 °C. We anticipate that based on our findings, the proposed strategy can potentially be evolved for novel materials with exceptional functionalities to fabricate highly efficient PCFCs and SOFCs.

## 2. Materials and Methods

### 2.1. Synthesis Procedures

The nanoparticles of ZnO were synthesized by following a three-step procedure. For this, the zinc acetate (ZnC<sub>4</sub>H<sub>6</sub>O<sub>4</sub>) was bought from Shanghai Macklin Biochemical Co., Ltd., Shanghai, China, at a purity level of up to 98.5%. At first, the zinc acetate was dissolved into deionized (DI) water, and a 0.1 mol/L solution was prepared. Similarly, 0.2 moles of Na<sub>2</sub>CO<sub>3</sub> were dissolved into 100 mL of DI water and poured drop-by-drop into the 0.1 mol/L solutions of ZnC<sub>4</sub>H<sub>6</sub>O<sub>4</sub> while stirring continuously. The resulting product was a milky white precipitate, which was further transferred into a Teflon autoclave for the hydrothermal treatment and placed at 180 °C for 12 h using a vacuum oven.

Consequently, the obtained fine suspension was washed with absolute ethanol/deionized water many times to avoid surface-adsorbed water. The obtained precursors were then dried via the dry freezing method for 4 h to evaporate the absorbed water. Lastly, the collected powders were calcined at 700 °C in air and afterward followed by reducing atmosphere (H<sub>2</sub>) at 550 °C for 4 h to obtain reduced nanoparticles of ZnO.

## 2.2. Characterizations Tools and Electrochemical Measurements

The structural crystallinity of the prepared ZnO nanoparticles was analyzed via X-ray diffraction using a Bruker D8 Advanced X-ray diffractometer (Bruker Corporation, Ettlingen, Germany) with Cu K $\alpha$  monochromator radiation at  $\lambda = 1.5418 \text{ \AA}$  in the  $2\theta$  range of  $10\text{--}70^\circ$  with a step size of  $0.2^\circ/\text{min}$ . At the same time, the FEI Tecnai G1 F30 device, JEOL JSM7100F high-resolution transmission electron microscope (HR-TEM), and a field emission scanning electron microscope (FE-SEM) were employed to investigate the microstructure, crystal structure, and chemical composition of synthesized ZnO. Furthermore, the chemical oxidation states were studied via X-ray photoelectron spectroscopy (XPS, Physical Electronics Quantum 2000, Al K $\alpha$  X-ray source). The raw data were fitted using CASA XPS software. The solar spectral absorption was measured using a UV-Vis 3600 spectrophotometer over a wavelength of  $200\text{--}800 \text{ nm}$ . A thermogravimetric analysis (TGA) was performed using a 449F3 simultaneous thermal analyzer in air atmospheres at  $30\text{--}800 \text{ }^\circ\text{C}$ .

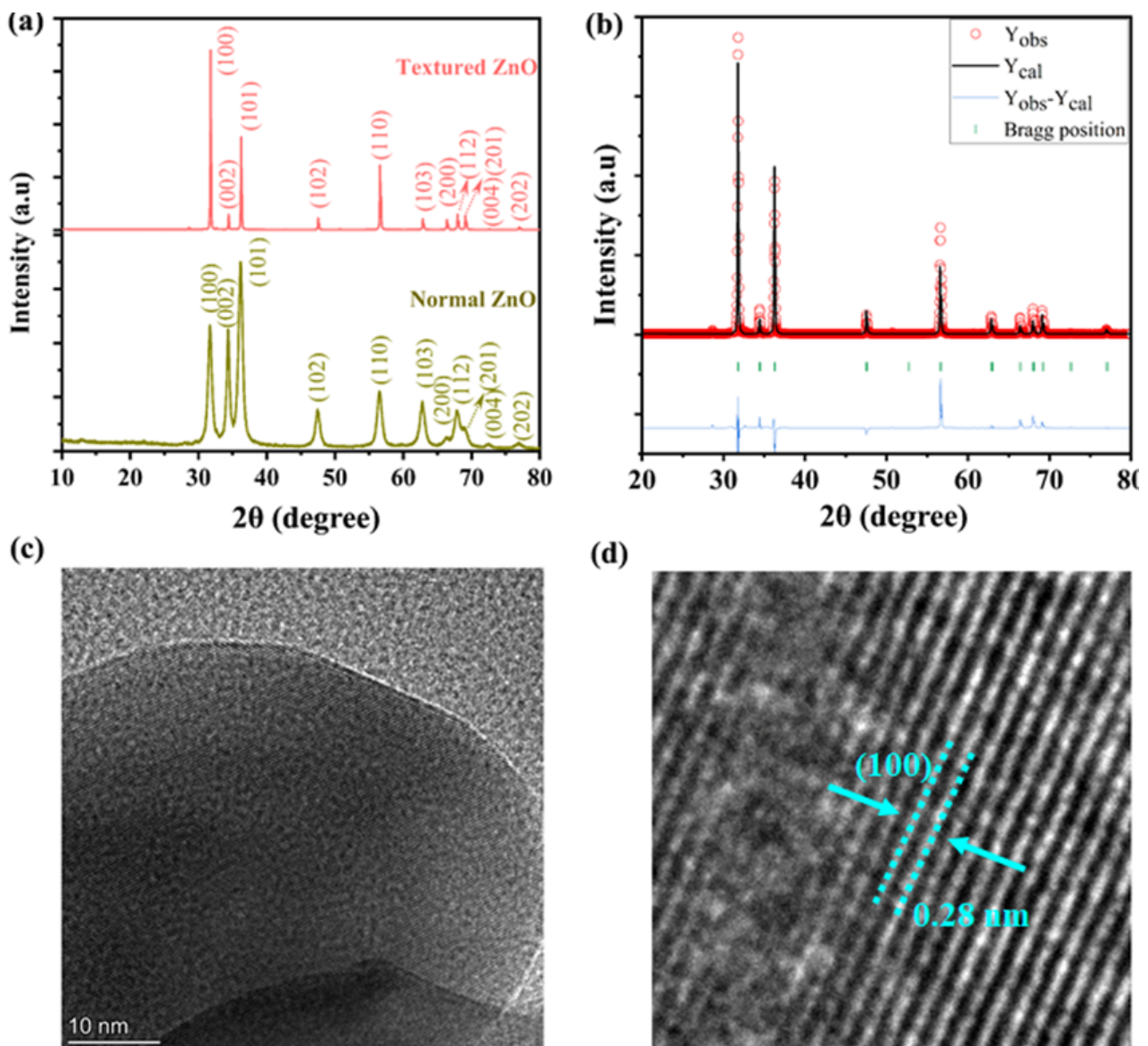
## 2.3. Complete Fabrication of Fuel Cells

Herein, we employed a simple one-step dry pressing technique to construct the solid fuel cell devices incorporating dense ZnO electrolytes and porous  $\text{Ni}_{0.8}\text{Co}_{0.15}\text{Al}_{0.05}\text{LiO}_{2-\delta}$  (NCAL) electrodes. In detail, the layered and structured NCAL powders acquired from Bamo Sci. and Tech. Joint Stock Company Ltd., Tianjin, China, were mixed into  $\text{C}_{10}\text{H}_{18}\text{O}$  to make a homogeneous slurry and painted with a brush onto porous Ni foam. Afterward, the NCAL-painted Ni-foam was dried in an oven at  $120 \text{ }^\circ\text{C}$  for 2 h for use as an electrode. Finally, synthesized ZnO nanoparticles and commercially acquired ZnO powders were pressed between two NCAL/Ni foam electrodes in a steel mold with a diameter of 13 mm (pressure, 240 Mpa) to obtain solid fuel cell devices with a total thickness of  $\cong 1.5 \text{ mm}$  and active area of  $0.64 \text{ cm}^2$ . The performance of the as-fabricated fuel cells was determined using the ITECH8511dc electronic load instrument (ITECH Electrical Co., Ltd., New Taipei, Taiwan), where  $\text{H}_2$  acts as the fuel and atmospheric air acts as the oxidant, with the flow rates of  $100\text{--}110 \text{ mL/min}$  and  $100 \text{ mL/min}$ , respectively. The obtained I-V and I-P curves of the measured data are presented here to show the electrochemical properties of the fabricated FC devices. A Gamry Reference 3000 (Warminster, PA, USA) workstation was used to measure electrochemical impedance spectroscopy (EIS) under an open-circuit voltage (OCV) with 10 mV of DC signal over the frequency range of 0.1 to  $10^6 \text{ Hz}$ . The recorded data were analyzed using ZSIMPWIN software.

## 3. Results

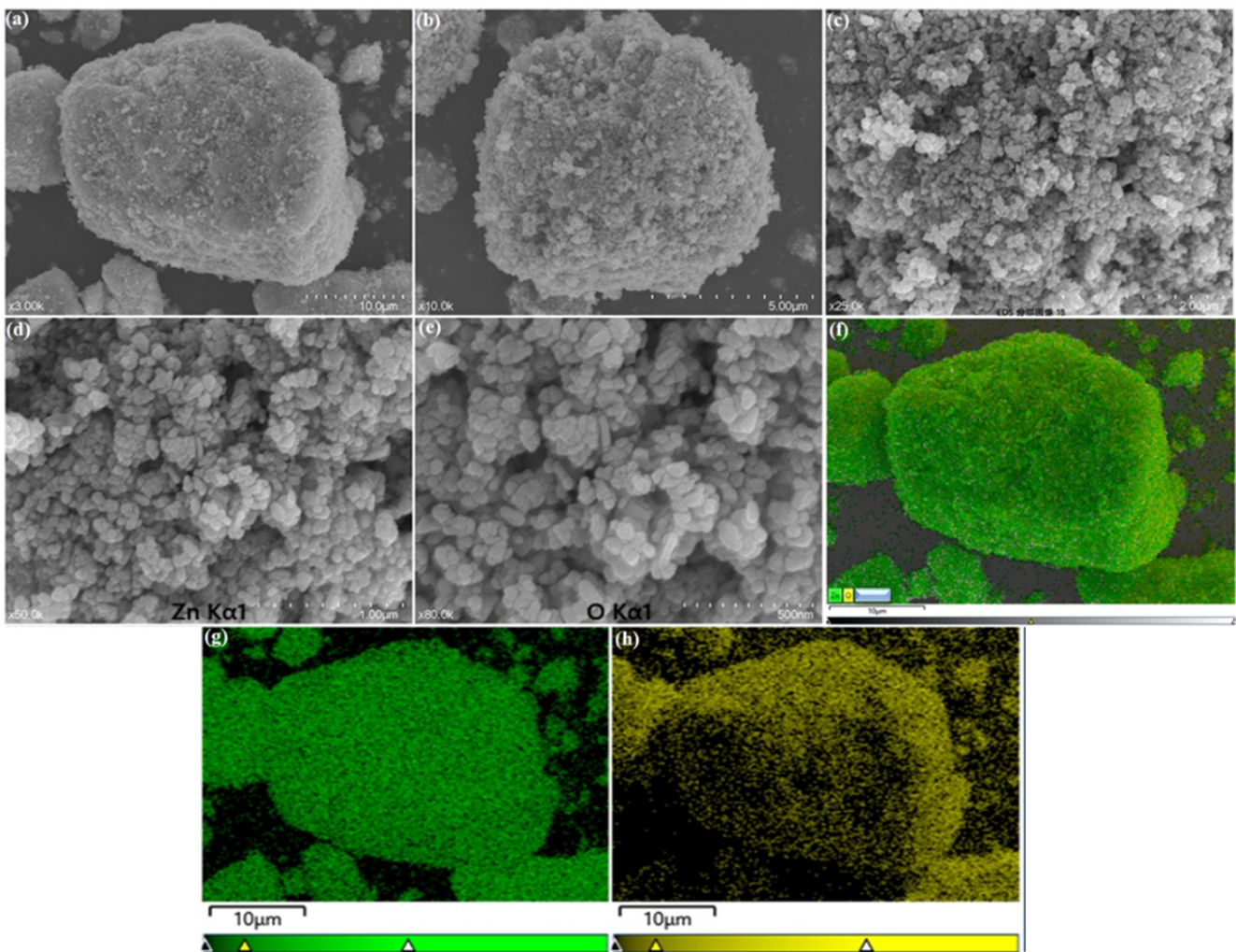
### 3.1. Structure and Composition Analysis

Figure 1a represents the X-ray diffraction patterns of pristine prepared ZnO nanoparticles and reduced ZnO, where key diffraction peaks are at  $2\theta^\circ$  positions of the 31, 34, 36, 47, 56, 62, 67, and 68, which can be identified as the (100), (002), (101), (102), (110), (103), and (112) planes, respectively, with hexagonal wurtzite-structured ZnO [14,15]. It is evident that there are no extra peaks in the patterns of ZnO nanoparticles rather than sharpening, which eliminates the possibility of additional phase formation after reducing into  $\text{H}_2$ , except for the wurtzite structure phase and a very small scattering at  $2\theta^\circ$  positions at 29 and 50, which possibly could be due to an impurity in the darning experiment. Moreover, the Rietveld refinement of the measured XRD data was achieved using Prof-Suit software for the ZnO nanoparticles, which showed a good fit to the experimental data and confirmed that the reduced ZnO particles had a hexagonal wurtzite structure, as shown in Figure 1b. To verify the crystallography of the synthesized ZnO nanorods, HR-TEM was used. Figure 1c,d shows an HR-TEM image, where the d-spacing value calculated using a digital micrograph is 0.28 nm, which can be assigned to the (100) plane [17–19].



**Figure 1.** (a) X-ray diffraction patterns of synthesized nanoparticles ZnO (b) after heating in the  $H_2$  atmosphere and (c,d) the crystal structure and d-spacing of the reduced ZnO particles measured via HR-TEM.

Figure 2 shows SEM images of the synthesized ZnO, revealing the sophisticated and fine surface morphology of the ZnO nanoparticles without any agglomeration. The fine growth of the ZnO particles and the imposition of agglomerates was achieved due to the purity of the synthesis method. Moreover, energy-dispersive spectroscopy (EDS) was employed to assess the elemental mapping. Figure 2f shows the combined chemical distribution mapping of ZnO at the particle level, revealing the uniform chemical distribution of the Zn (green color) and O (yellow color). Further, Figure 2g,h discloses the presence of each element (i.e., Zn and O) separately in the ZnO nanoparticles. The EDS spectra were also obtained to assess the elemental presence revealed in the EDS mapping, as shown in Figure 3, where overall percentages of 54.4% for Zn and 47.6% for O were observed. Hence, based on the mentioned results, the as-prepared ZnO particles correspond to the nano level and are well-aligned, leading towards surface area enhancements incorporating abundant active sites, which play a key role in the efficient performance of solid fuel cell devices [20–22].



**Figure 2.** (a–e) SEM images of ZnO at different scales. (f–h) EDS element mapping of synthesized ZnO nanoparticles.

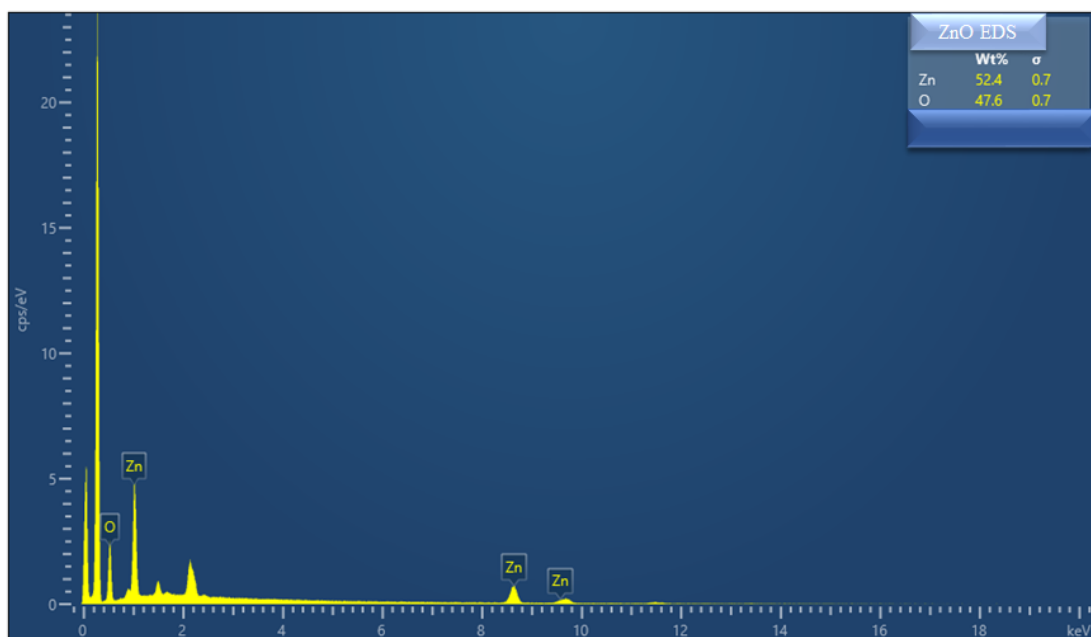


**Figure 3.** Energy-dispersive spectroscopy (EDS) spectrum of as-prepared ZnO nanoparticles.

### 3.2. Electrochemical Performance Measurements

For effective ion-conducting electrolytic performance in a fuel cell, the electrochemical properties of the prepared ZnO nanoparticles were compared to that of ZnO purchased commercially. The typical current-voltage (I-V) and associated power density (I-P) characteristics of fuel cells utilizing commercial ZnO and our synthesized ZnO material as an electrolyte operating at 550 °C are shown in Figure 4a. Our synthesized ZnO electrolyte demonstrated an OCV of 1.10 V and a maximum power density (Pmax) of 520 mW cm<sup>2</sup>, in contrast to the Pmax of only 320 mW cm<sup>2</sup> displayed by the ZnO that was purchased commercially, which was an appreciable improvement in electrochemical performance when operating at 550 °C [23–25]. Additionally, as shown in Figure 4b, our prepared ZnO electrolyte fuel cell showed excellent electrochemical performance even at low temperatures. At 500 °C and 450 °C, it showed peak power densities of 380 and 260 mW cm<sup>2</sup>, respectively. The improved electrochemical performance of the synthetic ZnO electrolyte over the commercially purchased ZnO particles points to the critical importance of the synthesis process and nanostructured morphology, in which the surface layer of ZnO could easily be reduced and could create a strong surface-oxygen-deficient layer structure to establish the surface path for the simple transport of H<sup>+</sup> when exposed to H<sub>2</sub> in fuel cell conditions [20]. Due to its high surface-active area and ease of surface layer reductions, the prepared ZnO material could help the electrochemical process by facilitating better proton intercalation. As a result, it can be concluded from the findings that the nanostructured stoichiometry of ZnO produced in three synthesis steps could be useful in controlling the structural properties of the surface. In this manner, the ZnO surface's heterolytic dissociation of H<sub>2</sub> to form Zn-H and O-H species is kinetically favored. With the reduction of the ZnO surface layer, the resulting Zn-H further evolves into the thermodynamically more stable O-H species.

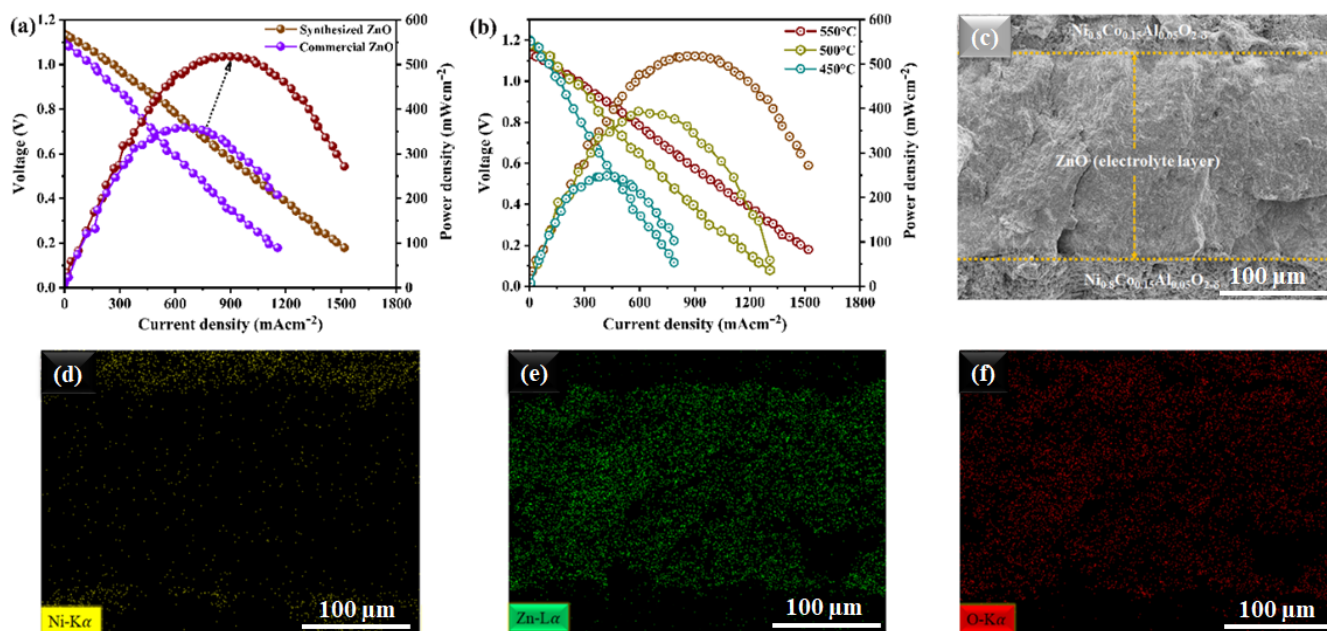


**Figure 4.** Characterization of the electrochemical performances: (a) characteristics curves of the typical current-voltage utilizing our ZnO nanoparticles and commercially purchased ZnO nanoparticles as electrolytes in fuel cells operated at 550 °C; (b) fuel cell performances using our prepared ZnO as an electrolyte under different operating temperatures of 450–550 °C; (c) cross-sectional SEM images of a tri-layer electrolyte-supported symmetrical fuel cell along with the prepared ZnO electrolyte examined after the electrochemical test; (d–f) EDS mapping of the ZnO electrolyte and Ni contents in the NCAL electrode.

Figure 4c illustrates the cross-sectional SEM image of a ZnO-based fuel cell before and after the operation, e.g., sintering and testing. It is evident from the SEM images that the fabricated ZnO electrolyte layer seems dense and tightly held with the adjacent anodes, without any cracks after the fuel cell performance operation. The adhesive and dense structure of the ZnO electrolyte could prevent gas leakage for better fuel cell performance [23,26]. Moreover, Figure 4d–f show the EDS mapping of the cross-sectional SEM images of the zinc-oxide-based fuel cells, where the distribution of Zn in the intermediate layer and Ni from the NCAL electrodes at the both edges of the cell can be seen.

### 3.3. Electrochemical Impedance and Electrical Conductivity

Additionally, EIS characterizations of the cells were carried out using a synthesized ZnO-nanoparticle-based electrolyte in an atmosphere of H<sub>2</sub> and air at 450–550 °C under OCV conditions. Figure 5a–c illustrates the Nyquist curves of the measured EIS spectra. The equivalent circuit modeling of R<sub>0</sub>-(R<sub>1</sub>-CPE<sub>1</sub>)-(R<sub>2</sub>-CPE<sub>2</sub>) was carried out using ZSIMPWIN software; here, R<sub>0</sub> is the ohmic resistance from the electrolyte and R<sub>1</sub> and R<sub>2</sub> are the charge transfer and mass transfer losses of the fuel cell with the ZnO electrolyte, respectively. The EIS spectra show that the R<sub>0</sub> of the fuel cell with ZnO significantly decreased in H<sub>2</sub>/air (fuel cell operating conditions) at a high temperature compared to low temperatures. For instance, the ZnO electrolyte fuel cell showed R<sub>0</sub> values of only 0.18 Ωcm<sup>2</sup> in H<sub>2</sub>/air at 550 °C and 0.78 Ωcm<sup>2</sup> at 450 °C. At low operating temperatures of 500 and 450 °C, a distinct difference in polarization loss (R<sub>1</sub> and R<sub>2</sub>) values was also noticeable. According to these findings, its surface may be reduced when ZnO is exposed to the H<sub>2</sub> atmosphere, and protons may move through this layer more easily. Then, as shown in Figure 5a–c, it dissolves the accumulation layer at the electrode–electrolyte interface, lowering the fuel cell’s charge transfer resistance (R<sub>1</sub>) and mass transport resistance (R<sub>2</sub>). The capacitance value may follow the decrease in mass and charge transfer values at each cell’s electrode–electrolyte interface. (i.e., R<sub>1</sub>~C<sub>1</sub>, R<sub>2</sub>~C<sub>2</sub>), where the capacitance can be determined by  $C_i = \frac{(R_i Q_i)^{1/n}}{R_i}$ , where R is the corresponding resistance and n is the frequency power [0 ≤ n ≤ 1] of the Q values [11,24,25,27]. The ionic conductivity of the synthesized ZnO in both fuel cells was evaluated using the R<sub>0</sub> values of the fitted data. As shown in Figure 5d, the ionic conductivity of the synthesized ZnO nanoparticles is 5.28 × 10<sup>-2</sup> S cm<sup>-1</sup>, which is much better at this operating temperature. Since it is difficult for oxygen ions or protons to move through bulk ZnO, the conductivity results confirm our findings that the ZnO surface may be reduced to deficient ZnO and may support rapid protonic transport. However, these results indicate that ZnO nanoparticles synthesized using three-step methods could be good candidates for electrolyte applications in advanced ceramic fuel cells [20].

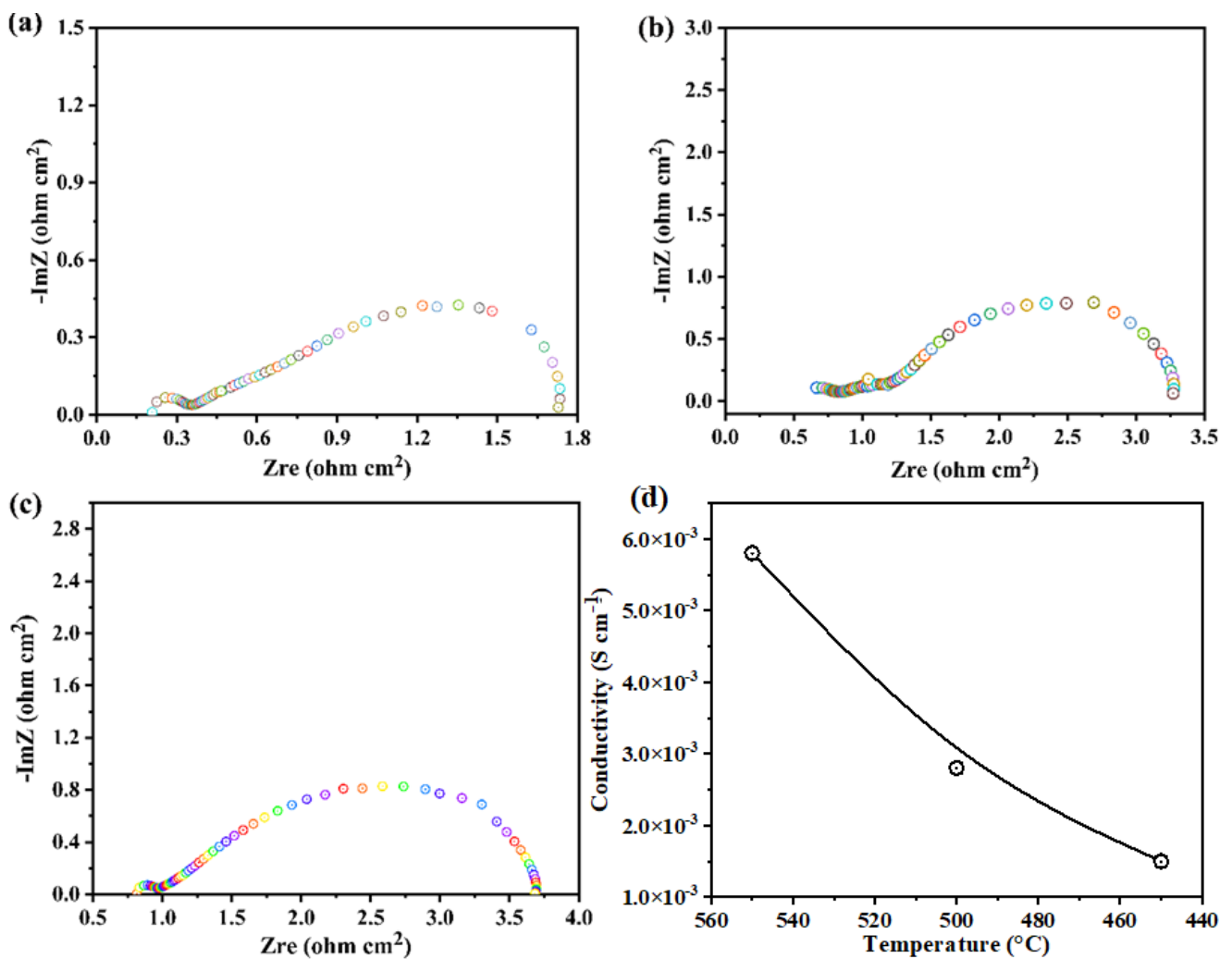


**Figure 5.** (a–c) Impedance spectra for the fuel cell prepared with the ZnO electrolyte layer measured in  $\text{H}_2/\text{air}$  at  $450\text{ }^{\circ}\text{C}$ – $550\text{ }^{\circ}\text{C}$ , respectively, where different colors represent the data measured at different frequency. (d) Measured ionic conductivity of the ZnO electrolyte at  $450$ – $550\text{ }^{\circ}\text{C}$ .

### 3.4. Spectroscopic Analysis

Additionally, a wide range of spectroscopic methods, including UV–visible, TGA, and X-ray photoelectron spectroscopy methods, were used to investigate additional structural characteristics of ZnO and reduced ZnO nanoparticle powders. The ZnO and reduced ZnO’s UV–visible absorbance spectra are shown in Figure 6a. It is possible to see a substantial difference in the absorbance spectra of the as-synthesized ZnO nanoparticles and reduced ZnO nanoparticles. The variations in absorbance spectra indicate that ZnO’s energy band gap is lower than the expected band gap ( $3.2\text{ eV}$ ); this is only possible because of the surface reduction and the creation of oxygen vacancies. This is widely reported when a large number of oxygen vacancies are produced, which also reduce the metal oxides’ energy band gaps [21,24,25,28].



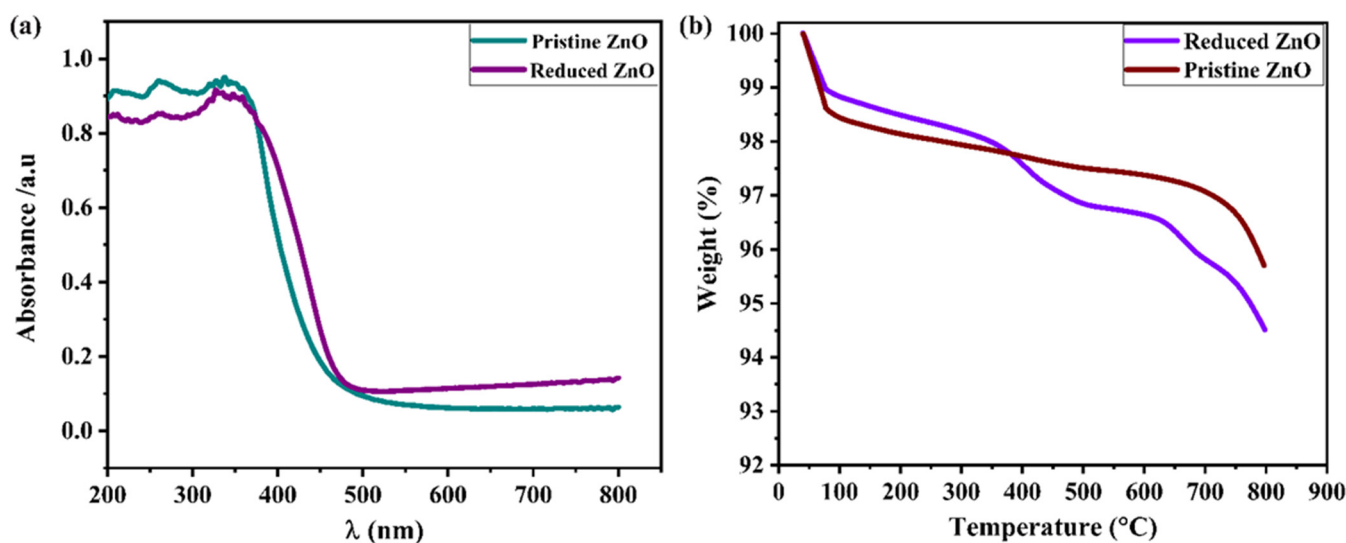
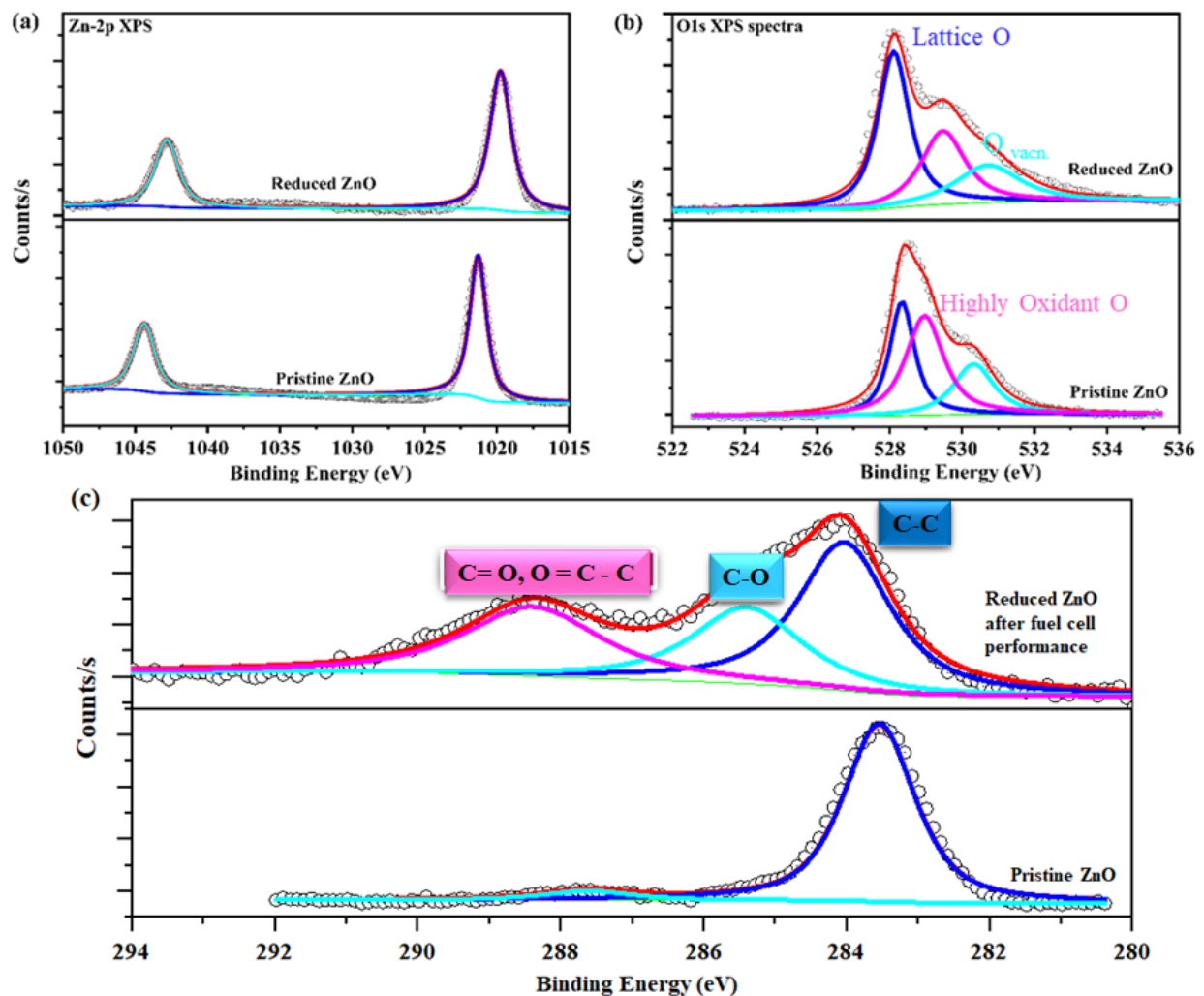


**Figure 6.** (a,b) UV-visible and TGA spectra of as-synthesized ZnO and reduced ZnO powders, respectively.

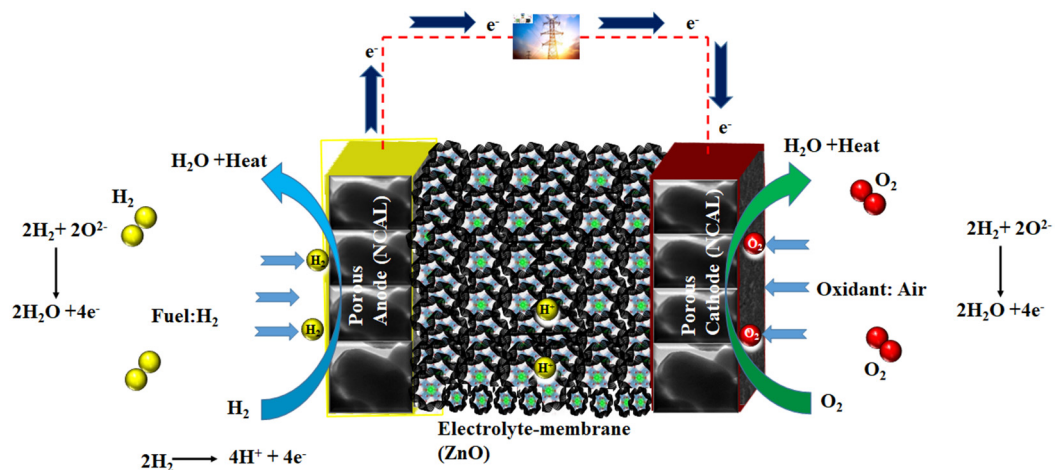
Moreover, the TGA was conducted in air at 30 to 800  $^{\circ}$ C to further investigate the effects of the reducing atmosphere on the ZnO nanoparticles, as demonstrated in Figure 6b. The evaporation of the absorbed water is indicated by the rapid weight loss in both samples around 100  $^{\circ}$ C. The other rapid weight changes begin at around 300  $^{\circ}$ C for the reduced ZnO nanoparticles, while the other rapid weight changes start at 500–600  $^{\circ}$ C to release lattice oxygen in the form of oxygen vacancies. The reduced ZnO sample exhibits the highest mass change, which is fully evident and supports our hypotheses. The large mass change in reduced ZnO nanoparticles could be released easily because of the softening of the Zn-O bands when exposed to H<sub>2</sub> and O.

Figure 7a,b demonstrates high-resolution XPS spectra of the as-synthesized and reduced ZnO powders. The high-resolution XPS spectra were fitted using a mixture of Lorentzian and Gaussian functions after Shirley's background was removed. Before the following electrochemical performance measurements, we were interested in observing the chemical and electronic state configuration changes of the Zn-2p, O1s, and C1s spectra. The XPS spectra of Zn-2p<sub>(1/2,3/2)</sub> are shown in Figure 7a. Before exposure to the H<sub>2</sub> atmosphere, they appear at a binding energy of 1022.32/1044.0 eV, while after exposure to the ZnO nanoparticles they appear at a binding energy of 1021.93/1043.22 eV. These shifts in B.E of Zn-2p<sub>(1/2,3/2)</sub> show a decrease in ZnO after exposure to H<sub>2</sub>. The Zn-2p structures presented an overall shift to lower binding energies, which is usually related to a non-stoichiometric formation. Additionally, a material's O1s spectra impact a material's ionic conductivity [29,30]. Lattice oxygen (O<sub>Lat.</sub>) and oxygen vacancy peaks can be seen in the O1s spectra following the fuel cell measurements, as depicted in Figure 6b. After exposure to a reducing atmosphere, the ZnO's O1s spectra show two partially superimposed peaks. Two significant excitations are present: the first involves lattice oxygen band O1s, while the second may be a deficient ZnO band with binding energies (B.E.) between 528 and 533.5 eV [28,29]. The oxygen lattice accounts for the low B.E. peak at 529.2 eV, while the additional oxygen vacancies account for the high B.E. peak at 531.42 eV. Increased oxygen vacancies, which are crucial for high fuel cell performance, are indicated by an enhanced area percentage ratio for O<sub>Lat.</sub>/O<sub>Vac</sub> in the reduced ZnO [21,28]. Moreover, as demonstrated in Figure 8, these findings demonstrate that an in-situ surface reduction creates oxygen vacancies for fast proton transport. As a result, our developed method may offer a new approach to producing high-performance LT-SOFC electrolyte materials [31]. This indicates that the ZnO seems to have more oxygen vacancies than pristine ZnO after the fuel cell performance measurements. Figure 8 illustrates a schematic illustration of

the process for configuring a deficient ZnO layer necessary for the mobility of oxygen and proton ions.



**Figure 7.** (a–c) X-ray photoelectron spectra of the Zn-2p, O1s, and C1s spectra of as-synthesized ZnO powders after fuel cell performance measurements, where different colors represent various peaks of XPS spectra.



**Figure 8.** The electrochemical processes involved in the phase transition of ZnO to deficient ZnO for ionic transport in the operation of a zinc-oxide-based fuel cell.

Previous studies have demonstrated that ceramic fuel cells using  $\text{Ni}_{0.8}\text{Co}_{0.15}\text{Al}_{0.05}\text{LiO}_2$  (NCAL) symmetrical electrodes exhibit good electrochemical performance in the temperature range of 450 to 600 °C. NCAL at the anode side is reduced by  $\text{H}_2$  to produce  $\text{Li}_2\text{CO}_3$  or a lithium hydro-oxide (LiOH) species mixture and diffuses into the electrolyte part, which causes high ionic conductivity throughout the electrolyte layer [31]. In this way, the LiOH or  $\text{Li}_2\text{CO}_3$  is produced by the NCAL after  $\text{H}_2$  reduction and after diffusing the electrolyte particles and forms a core-shell composite electrolyte. However, the partial melting and softening of  $\text{Li}_2\text{CO}_3/\text{LiOH}$  in the operating temperature range of 450–500 °C could be the main reason for the high performance of the ZnO-based fuel cell, as shown in Figure 7c (C1s spectra). A similar mechanism is also reported for  $\text{CeO}_2$ ,  $\text{TiO}_2$ , and  $\text{ZrO}_2$  [31]. According to the final step in Figure 8, the proton transport is associated with a layer of ZnO particles on the surface.

#### 4. Conclusions

We successfully combined three synthesis techniques to prepare and characterize a ZnO-nanostructured material. Moreover, due to the hexagonal wurtzite nanostructure, the synthetic nanostructured ZnO exhibits exceptional ionic conductivity during fuel cell operation. The ionic conductivity was  $5.28 \times 10^{-2} \text{ S cm}^{-1}$ , which is high. At 550 °C, the fuel cell with the prepared ZnO as the electrolyte demonstrated a high-power density of  $520 \text{ mW cm}^2$ . Additionally, we investigated the mechanism underlying the upsurge in ionic conductivity of the reduced ZnO nanoparticles during fuel cell operation using various microscopic and spectroscopic analyses. We noticed that the synthetic nanostructured ZnO surfaces are quickly reduced to form an oxygen-deficient layer and to efficiently expedite proton transport when exposed to a reduced atmosphere. Our findings and the characteristics of the ZnO's structural changes were clearly described by the ex-situ spectroscopy results, which included EIS, UV-visible, XPS, and TGA methods. In conclusion, this technique might be the inspiration for the formation of novel proton-conducting electrolytes and oxides based on zinc oxide, which may benefit all energy devices and material systems.

**Author Contributions:** The conceptualization of this work was completed by J.L. and Y.L. The methodology was completed by N.M. and M.A.K.Y.S. The formal analysis and investigation were completed by N.A. and M.S.L., while R.Y. and S.Y. provided the resources and data curation facilities. J.L. prepared original draft which was reviewed and edited by N.M. and Y.L. All authors have read and agreed to the published version of the manuscript.

**Funding:** We thank the Department of Electronic Engineering, Huainan Union University, Huainan, China; and the School of Electronic Engineering, Nanjing Xiaozhuang University, Nanjing, China, for providing the experimental facilities. Further, this work was supported by the National Natural Science Foundation of China (NSFC) under grant numbers 51772080 and 11604088 and Southeast University (SEU PROJET # 3203002003A2).

**Institutional Review Board Statement:** Not applicable.

**Informed Consent Statement:** These studies not involving any humans.

**Data Availability Statement:** The data that support the findings of this study are available from the corresponding authors upon reasonable request.

**Acknowledgments:** The authors acknowledge the Department of Electronic Engineering, Huainan Union University, Huainan, China and School of Electronics and Engineering, Nanjing Xiaozhuang University, Nanjing, China for providing the experimental facilities and covering the publication charges.

**Conflicts of Interest:** The authors declare no conflict of interest.

#### References

1. Duan, C.; Kee, R.J.; Zhu, H.; Karakaya, C.; Chen, Y.; Ricote, S.; Jarry, A.; Crumlin, E.J.; Hook, D.; Braun, R.; et al. Highly durable, coking and sulfur tolerant, fuel-flexible protonic ceramic fuel cells. *Nature* **2018**, *557*, 217–222. [[CrossRef](#)] [[PubMed](#)]
2. Choi, S.; Kucharczyk, C.J.; Liang, Y.; Zhang, X.; Takeuchi, I.; Ji, H.-I.; Haile, S.M. Exceptional power density and stability at intermediate temperatures in protonic ceramic fuel cells. *Nat. Energy* **2018**, *3*, 202–210. [[CrossRef](#)]

3. Malavasi, L.; Fisher, C.A.J.; Islam, M.S. Oxide-ion and proton conducting electrolyte materials for clean energy applications: Structural and mechanistic features. *Chem. Soc. Rev.* **2010**, *39*, 4370–4387. [[CrossRef](#)]
4. Goodenough, J.B. Oxide-Ion Conductors by Design. *Nature* **1999**, *404*, 821–823. [[CrossRef](#)] [[PubMed](#)]
5. Zhang, L.; Chae, S.-R.; Hendren, Z.; Park, J.-S.; Wiesner, M.R. Recent advances in proton exchange membranes for fuel cell applications. *Chem. Eng. J.* **2012**, *204–206*, 87–97. [[CrossRef](#)]
6. Bi, L.; Da'As, E.H.; Shafi, S.P. Proton-conducting solid oxide fuel cell (SOFC) with Y-doped BaZrO<sub>3</sub> electrolyte. *Electrochem. Commun.* **2017**, *80*, 20–23. [[CrossRef](#)]
7. Hakim, M.; Yoo, C.-Y.; Joo, J.H.; Yu, J.H. Enhanced durability of a proton conducting oxide fuel cell with a purified yttrium-doped barium zirconate-cerate electrolyte. *J. Power Sources* **2015**, *278*, 320–324. [[CrossRef](#)]
8. Muccillo, R.; Muccillo, E.N. Synthesis and Properties of BaZr<sub>0.1</sub>Ce<sub>0.7</sub>Y<sub>2-x</sub>M<sub>x</sub>O<sub>3-δ</sub> (x = 0, 0.1; M = Dy, Yb) Compounds. *ECS Trans.* **2011**, *35*, 1251. [[CrossRef](#)]
9. Liu, Z.; Zhou, M.; Chen, M.; Cao, D.; Shao, J.; Liu, M.; Liu, J. A high-performance intermediate-to-low temperature protonic ceramic fuel cell with in-situ exsolved nickel nanoparticles in the anode. *Ceram. Int.* **2020**, *46*, 19952–19959. [[CrossRef](#)]
10. Shah, M.Y.; Mushtaq, N.; Rauf, S.; Akbar, N.; Xing, Y.; Wu, Y.; Wang, B.; Zhu, B. Advanced fuel cell based on semiconductor perovskite La–BaZrYO<sub>3-δ</sub> as an electrolyte material operating at low temperature 550 °C. *Int. J. Hydrogen Energy* **2020**, *45*, 27501–27509. [[CrossRef](#)]
11. Shah, M.A.K.Y.; Rauf, S.; Mushtaq, N.; Zhu, B.; Tayyab, Z.; Yousaf, M.; Hanif, M.B.; Lund, P.D.; Lu, Y.; Asghar, M.I. Novel Perovskite Semiconductor Based on Co/Fe-Co-doped LBZY (La<sub>0.5</sub>Ba<sub>0.5</sub>Co<sub>0.2</sub>Fe<sub>0.2</sub>Zr<sub>0.3</sub>Y<sub>0.3</sub>O<sub>3-δ</sub>) as an Electrolyte in Ceramic Fuel Cells. *ACS Appl. Energy Mater.* **2021**, *4*, 5798–5808. [[CrossRef](#)]
12. Lu, Y.; Mi, Y.; Li, J.; Qi, F.; Yan, S.; Dong, W. Recent Progress in Semiconductor-Ionic Conductor Nanomaterial as a Membrane for Low-Temperature Solid Oxide Fuel Cells. *Nanomaterials* **2021**, *11*, 2290. [[CrossRef](#)] [[PubMed](#)]
13. Xia, C.; Mi, Y.; Wang, B.; Lin, B.; Chen, G.; Zhu, B. Shaping triple-conducting semiconductor BaCo<sub>0.4</sub>Fe<sub>0.4</sub>Zr<sub>0.1</sub>Y<sub>0.1</sub>O<sub>3-δ</sub> into an electrolyte for low-temperature solid oxide fuel cells. *Nat. Commun.* **2019**, *10*, 1707. [[CrossRef](#)] [[PubMed](#)]
14. Shah, M.A.; Mushtaq, N.; Rauf, S.; Xia, C.; Zhu, B. The semiconductor SrFe<sub>0.2</sub>Ti<sub>0.8</sub>O<sub>3-δ</sub>-ZnO heterostructure electrolyte fuel cells. *Int. J. Hydrogen Energy* **2019**, *44*, 30319–30327. [[CrossRef](#)]
15. Xia, C.; Qiao, Z.; Shen, L.; Liu, X.; Cai, Y.; Xu, J.; Wang, H. Semiconductor electrolyte for low-operating-temperature solid oxide fuel cell: Li-doped ZnO. *Int. J. Hydrogen Energy* **2018**, *43*, 12825–12834. [[CrossRef](#)]
16. Xia, C.; Qiao, Z.; Feng, C.; Kim, J.-S.; Wang, B.; Zhu, B. Study on Zinc Oxide-Based Electrolytes in Low-Temperature Solid Oxide Fuel Cells. *Materials* **2018**, *11*, 40. [[CrossRef](#)] [[PubMed](#)]
17. Stevens, J.; Wiczorek, W.; Raducha, D.; Jeffrey, K. Proton conducting gel/H<sub>3</sub>PO<sub>4</sub> electrolytes. *Solid State Ion.* **1997**, *97*, 347–358. [[CrossRef](#)]
18. Yashima, M.; Tsujiguchi, T.; Sakuda, Y.; Yasui, Y.; Zhou, Y.; Fujii, K.; Torii, S.; Kamiyama, T.; Skinner, S.J. High Oxide-Ion Conductivity through the Interstitial Oxygen Site in Ba<sub>7</sub>Nb<sub>4</sub>MoO<sub>20</sub>-Based Hexagonal Perovskite Related Oxides. *Nat. Commun.* **2021**, *12*, 556. [[CrossRef](#)]
19. Wang, B.B.; Zhong, X.X.; He, C.L.; Zhang, B.; Cvelbar, U.; Ostrikov, K. Solvent-dependent structures and photoluminescence of WO<sub>3-x</sub> nanomaterials grown in nonaqueous solutions. *J. Alloys Compd.* **2021**, *854*, 157249. [[CrossRef](#)]
20. Wang, Z.; Fan, X.; Li, C.; Men, G.; Han, D.; Gu, F. Humidity-sensing performance of 3DOM WO<sub>3</sub> with controllable structural modification. *ACS Appl. Mater. Interfaces* **2018**, *10*, 3776–3783. [[CrossRef](#)]
21. Shah, M.Y.; Rauf, S.; Zhu, B.; Mushtaq, N.; Yousaf, M.; Lund, P.D.; Xia, C.; Asghar, M.I. Semiconductor Nb-Doped SrTiO<sub>3-δ</sub> Perovskite Electrolyte for a Ceramic Fuel Cell. *ACS Appl. Energy Mater.* **2021**, *4*, 365–375. [[CrossRef](#)]
22. Mushtaq, N.; Xia, C.; Dong, W.; Wang, B.; Raza, R.; Ali, A.; Afzal, M.; Zhu, B. Tuning the energy band structure at interfaces of the SrFe<sub>0.75</sub>Ti<sub>0.25</sub>O<sub>3-δ</sub>-Sm<sub>0.25</sub>Ce<sub>0.75</sub>O<sub>2-δ</sub> heterostructure for fast ionic transport. *ACS Appl. Mater. Interfaces* **2019**, *11*, 38737–38745. [[CrossRef](#)] [[PubMed](#)]
23. Wang, B.; Cai, Y.; Xia, C.; Kim, J.S.; Liu, Y.; Dong, W.; Wang, H.; Afzal, M.; Li, J.; Raza, R.; et al. Semiconductor-ionic membrane of LaSrCoFe-oxide-doped ceria solid oxide fuel cells. *Electrochim. Acta* **2017**, *248*, 496–504. [[CrossRef](#)]
24. Shah, M.A.K.Y.; Zhu, B.; Rauf, S.; Mushtaq, N.; Yousaf, M.; Ali, N.; Tayyab, Z.; Akbar, N.; Yang, C.P.; Wang, B. Electrochemical properties of a co-doped SrSnO<sub>3-δ</sub>-based semiconductor as an electrolyte for solid oxide fuel cells. *ACS Appl. Energy Mater.* **2020**, *3*, 6323–6333. [[CrossRef](#)]
25. Mushtaq, N.; Lu, Y.; Xia, C.; Dong, W.; Wang, B.; Shah, M.Y.; Rauf, S.; Akbar, M.; Hu, E.; Raza, R.; et al. Promoted electrocatalytic activity and ionic transport simultaneously in dual functional Ba<sub>0.5</sub>Sr<sub>0.5</sub>Fe<sub>0.8</sub>Sb<sub>0.2</sub>O<sub>3-δ</sub>-Sm<sub>0.2</sub>Ce<sub>0.8</sub>O<sub>2-δ</sub> heterostructure. *Appl. Catal. B Environ.* **2021**, *298*, 120503. [[CrossRef](#)]
26. Shah, M.Y.; Tayyab, Z.; Rauf, S.; Yousaf, M.; Mushtaq, N.; Imran, M.A.; Lund, P.D.; Asghar, M.I.; Zhu, B. Interface engineering of bi-layer semiconductor SrCoSnO<sub>3-δ</sub>-CeO<sub>2-δ</sub> heterojunction electrolyte for boosting the electrochemical performance of low-temperature ceramic fuel cell. *Int. J. Hydrogen Energy* **2021**, *46*, 33969–33977. [[CrossRef](#)]
27. Chen, G.; Liu, H.; He, Y.; Zhang, L.; Asghar, M.I.; Geng, S.; Lund, P.D. Electrochemical mechanisms of an advanced low-temperature fuel cell with a SrTiO<sub>3</sub> electrolyte. *J. Mater. Chem. A* **2019**, *7*, 9638–9964. [[CrossRef](#)]
28. Katrib, A.; Hemming, F.; Wehrer, P.; Hilaire, L.; Maire, G. The multi-surface structure and catalytic properties of partially reduced WO<sub>3</sub>, WO<sub>2</sub> and WC + O<sub>2</sub> or W + O<sub>2</sub> as characterized by XPS. *J. Electron Spectrosc. Relat. Phenom.* **1995**, *76*, 195–200. [[CrossRef](#)]

29. Efkere, H.I.; Gümrükçü, A.E.; Özen, Y.; Kınacı, B.; Aydın, S.Ş.; Ates, H.; Özçelik, S. Investigation of the effect of annealing on the structural, morphological and optical properties of RF sputtered WO<sub>3</sub> nanostructure. *Phys. B Condens. Matter*. **2021**, *622*, 413350. [[CrossRef](#)]
30. Wang, B.; Zhu, B.; Yun, S.; Zhang, W.; Xia, C.; Afzal, M.; Cai, Y.; Liu, Y.; Wang, Y.; Wang, H. Fast ionic conduction in semiconductor CeO<sub>2-δ</sub> electrolyte fuel cells. *NPG Asia Mater.* **2019**, *11*, 51. [[CrossRef](#)]
31. Ruixin, D.; Gang, C.; Kai, W.; Zhuo, C.; Xiaohong, L.; Guoqiang, L.; Ying, L.; Shujiang, G. Effect of chemical reactions between electrolyte and lithium compounds on the electrochemical performance of the ceramic fuel cells. *Carbon Resour. Convers.* **2022**, *5*, 131–138.